Received: Added at production | Revised: Added at production | Accepted: Added at production

DOI: xxx/xxxx

ARTICLE TYPE

Tetrahedral adaptive mesh refinement for two-phase flows using conservative level-set method.

Oscar Antepara*[1,2] | Néstor Balcázar[2] | Assensi Oliva*[1]

[1]Heat and Mass Transfer Technological Center (CTTC), Universitat Politècnica de Catalunya - BarcelonaTech (UPC), ESEIAAT, Colom 11, 08222 Terrassa, Barcelona, Spain

[2]Termo Fluids, S.L., Avda Jacquard 97 1-E, 08222 Terrassa, Barcelona, Spain

Correspondence
*Oscar Antepara, Email: oscar@cttc.upc.edu, oscarantepara@gmail.com.

Assensi Oliva, Email: cttc@cttc.upc.edu. Fax: +(34) 93 739 89 20

Present Address
Oscar Antepara - Center for Computational Sciences and Engineering, Lawrence Berkeley National Laboratory, 1 Cyclotron Road, MS 50A-3111 Berkeley, CA 94720, USA, Email: oantepara@lbl.gov

Néstor Balcázar - School of Engineering, Newcastle University, Claremont Road, Newcastle-Upon-Tyne NE1 7RU, UK

Summary

In this paper, we describe a parallel adaptive mesh refinement strategy for two-phase flows using tetrahedral meshes. The proposed methodology consists of combining a conservative level-set method with tetrahedral adaptive meshes within a finite volume framework. Our adaptive algorithm applies a cell-based refinement technique and adapts the mesh according to physics-based refinement criteria defined by the two-phase application. The new adapted tetrahedral mesh is obtained from mesh manipulations of an input mesh: operations of refinement and coarsening until a maximum level of refinement is achieved. For the refinement method of tetrahedral elements, geometrical characteristics are taking into consideration to preserve the shape quality of the subdivided elements. The present method is used for the simulation of two-phase flows, with surface tension, to show the capability and accuracy of 3D adapted tetrahedral grids to bring new numerical research in this context. Finally, the applicability of this approach is shown in the study of the gravity-driven motion of a single bubble/droplet in a quiescent viscous liquid on regular and complex domains.

KEYWORDS:
Adaptive mesh refinement, tetrahedral mesh, finite-volume method, tetrahedral elements, conservative level-set, multiphase flows

1 | INTRODUCTION

Applications in the nuclear, chemical and nano industry involving coiled flow tubes or micro-devices lead to the challenge of designing systems of two-phase flows where the systems present complex geometries [1]. Computationally modeling these systems are a challenging topic due to the multi-scale nature of this phenomenon. A good strategy to efficiently solve these problems is the use of numerical algorithms for unstructured meshes, where governing equations of two-phase flows can be accurately solved in complex computational domains. Therefore, the primary purpose of this work is the development of a finite-volume tetrahedral adaptive mesh refinement algorithm for two-phase flows, with surface tension, in complex domains.

Two-phase flows modeling requires numerical tools to properly identify the interface between fluids. On this context, interface capturing methods have been developed for Direct numerical simulation (DNS) of multiphase applications such as bubbles, droplets, or jets. In the literature, we can find the Front Tracking method (FT)[2,3], Volume-of-Fluid (VOF)[4,5,6], Standard Level-Set (LS)[7,8,9], coupled VOF-LS[10,11,12,13] and Conservative Level-Set (CLS)[14,15,16] as some of the most common methodologies used for interface capturing. Even though each method has its advantages and disadvantages, one of the main issues that can arise is the mass conservation of fluid phases and accurate computation of curvatures. Lately, a finite-volume CLS method for two-phase flows on unstructured grids with surface tension has been proposed by Balcázar *et al.* [16], and further extended to interfacial

flows with variable surface tension[13], bubbly flows[17,18,19,20], and interfacial heat/mass transfer[19,20]. Whereas the finite-volume approach leads to the satisfaction of the integral forms of the conservation laws over the entire domain, the unstructured CLS method has further advantages such as numerical stability at high physical properties ratios (density and viscosity), mass conservation of fluid phases, accurate computation of surface tension, and efficient parallelization, as demonstrated in our previous works[16,18,21,13,17,19,20].

A shortcoming on two-phase flows modeling is the extensive use of computational resources on tetrahedral grids, where most of the grid elements should be near the interface between phases. This issue can be solved with the use of Adaptive Mesh Refinement (AMR), initially introduced by[22,23,24], where enough grid resolution can be achieved following a refinement/coarsening criteria. Several methods have been developed concerning the AMR for triangular and tetrahedral meshes using bisection, re-meshing and regular refinement, where an overview of the advances on this topic during the recent years can be found in[25]. On the context of using AMR for tetrahedral meshes for multiphase and turbulent problems, many authors have developed some methods for the applications mentioned above. For single-phase flows[26,27,28] proposed an unstructured adaptive meshing method for finite element discretization using error control. Moreover, unstructured adaptive refinement with level-set methods were developed using adaptive re-meshing with finite volume[29,30,31,32] and finite element[33,34] discretization methods. In addition, element subdivision methods have been developed on unstructured meshes for different discretization methods, being the finite element the most widely applied[35,36,37,38], which have been used for different applications. One concern around these methods is the resulting non-conforming meshes which have been solved with algorithms to ensure a conforming mesh. Another issue is the mesh quality resulting from the refinement methods, which is of importance due to poor quality elements can produce numerical errors in the solution procedure[39,40]. A solution to this problem is the use of specific geometric criteria on the selection of the refinement mechanism that will lead to a quality change bounded to certain limits[41]. Furthermore, the main limitations on tetrahedral AMR are the achievement of accurate and non-expensive 3D simulations, the application of this methodology to unsteady problems, the diminishing of the mesh quality that can introduce numerical errors and the use of conforming meshes.

In this work, we want to present a new methodology which incorporates a parallel AMR method for tetrahedral meshes on a finite-volume framework for two-phase flows on collocated unstructured meshes. This approach allows the use of regular refinement and non-conformed meshes. Moreover, a process to ensure an optimal tetrahedral quality, during the refinement step, will be followed. Finally, this method will be tested in the solution of two-phase flows, involving surface tension, using a conservative level set method on regular and complex domains.

The paper is organized as follows. The mathematical formulation and the numerical method used are described in Section 2. The Adaptive Mesh Refinement algorithm for tetrahedral meshes is described in Section 3. Validations with the simulation of a gravity-driven bubble/droplet on complex domains are discussed in Section 4. Section 5 summarizes the numerical method and the results outlined in the paper.

2 | MATHEMATICAL MODEL AND NUMERICAL METHODS

2.1 | Incompressible two-phase flow

The governing equations for momentum and mass conservation of two immiscible incompressible and Newtonian fluids are given by the Navier-Stokes equations defined for the so-called one-fluid formulation[42,43,44,3,16]:

$$\frac{\partial}{\partial t}(\rho \mathbf{v}) + \nabla \cdot (\rho \mathbf{v}\mathbf{v}) = -\nabla p + \nabla \cdot \mu \left(\nabla \mathbf{v} + (\nabla \mathbf{v})^T\right) + \rho \mathbf{g} + \sigma \kappa \mathbf{n} \delta_\Gamma, \tag{1}$$

$$\nabla \cdot \mathbf{v} = 0, \tag{2}$$

where μ is dynamic viscosity, ρ is density, p is pressure, $\mathbf{v}$ is velocity field, $\mathbf{g}$ is gravity acceleration, the super-index T represents the transpose operator, δ_Γ is a Dirac delta function at the interface Γ, σ is the surface tension coefficient, κ is the curvature of the interface, and $\mathbf{n}$ denotes the normal unit vector on the interface. Moreover, physical parameters vary across the interface, as follows:

$$\begin{aligned} \rho &= \rho_1 H_1 + \rho_2 (1 - H_1) \\ \mu &= \mu_1 H_1 + \mu_2 (1 - H_1), \end{aligned} \tag{3}$$

with μ_1, μ_2 and ρ_1, ρ_2 being the viscosities and densities of both fluids, respectively. H_1 is the Heaviside step function defined as one at fluid 1, and zero elsewhere. Furthermore, physical properties are smoothed following the CLS method for unstructured meshes at the discretized level[16].

2.2 | Conservative level set, surface tension and regularization of fluid properties

The CLS method[14,16], as introduced by Balcázar *et al.*[16] in the framework of the finite-volume approach and unstructured meshes is employed in this research. The CLS method uses a regularized indicator function, ϕ:

$$\phi(\mathbf{x},t) = \frac{1}{2}\left(tanh\left(\frac{d(\mathbf{x},t)}{2\varepsilon}\right)+1\right), \tag{4}$$

where $d(\mathbf{x},t)$ is a signed distance function[8], $\varepsilon = 0.5h^{0.9}$ sets the profile thickness, h is the local grid size defined in this work as the average distance between the local cell-centroid and neighbor cell-centroids with common face around the local cell[19]. The interface Γ is defined by the iso-surface $\phi = 0.5$:

$$\Gamma = \{\mathbf{x} \mid \phi(\mathbf{x},t) = 0.5\}. \tag{5}$$

Since the conservative level-set function is advected by the fluid velocity field, an interface transport equation is required:

$$\frac{\partial \phi}{\partial t} + \nabla \cdot \phi \mathbf{v} = 0. \tag{6}$$

The conservative level-set function must be reinitialized to keep a constant interface thickness and profile, with the next equation[16]:

$$\frac{\partial \phi}{\partial \tau} + \nabla \cdot \phi(1-\phi)\mathbf{n}|_{\tau=0} = \nabla \cdot \varepsilon \nabla \phi, \tag{7}$$

which is advanced for the pseudo-time τ up to achieve the steady state. The compressive term, $\nabla \cdot \phi(1-\phi)\mathbf{n}|_{\tau=0}$, compress the CLS function along the interface normal vector ($\mathbf{n}|_{\tau=0}$). The diffusion term, $\nabla \cdot \varepsilon \nabla \phi$, keeps the CLS profile with a thickness proportional to ε (see Eq.(4)). As introduced in[16], ε is included inside the divergence operator. Indeed, at the discretized level its value at cell-faces (ε_f) is linearly interpolated. The surface tension force at the interface is modeled via the continuous surface force model (CSF)[43]. Therefore, $\sigma\kappa\mathbf{n}\delta_\Gamma$ is turned to a volume force as follows[16,13]:

$$\sigma\kappa\mathbf{n}\delta_\Gamma = \sigma\kappa(\phi)\nabla\phi, \tag{8}$$

where $\kappa(\phi)$ and $\mathbf{n}$ are given by

$$\mathbf{n} = \frac{\nabla\phi}{||\nabla\phi||}, \tag{9}$$

$$\kappa(\phi) = -\nabla \cdot \mathbf{n}. \tag{10}$$

As proposed by [16,13,19], curvature is computed at the cell Ω_P as $\kappa_P = -V_P^{-1}\sum_f \mathbf{n}_f \cdot \mathbf{A}_f$, where f denotes the faces on the surface of Ω_P, subindex P denotes the current cell, $\mathbf{A}_f$ is the face-area vector pointing outside Ω_P, and V_P is the volume of Ω_P. Finite-volume discretization of surface tension force (Eq.(8)), as well as technical details on the regularization of the Dirac delta function, are reported in our previous works[19,13,16]. Finally, fluid properties are regularized using the level-set function, as follows,

$$\begin{aligned}\rho &= \rho_1\phi + \rho_2(1-\phi),\\ \mu &= \mu_1\phi + \mu_2(1-\phi).\end{aligned} \tag{11}$$

The reader is referred to[16,13,19] for further details on the unstructured CLS method used in this work.

2.3 | Numerical methods

The governing equations have been discretized by a finite-volume (FV) approach on collocated unstructured meshes as first introduced by[16,13,17,19], which is coupled with the tetrahedral AMR framework. In what follows, the numerical approach is reviewed for the sake of completeness.

The convective term of momentum equation (Eq.(12)) and interface transport equation (Eq.(6)), $\nabla_h \cdot (\beta\psi\mathbf{v})$, is discretized by a Total Variation Diminishing (TVD) Superbee flux-limiter scheme for unstructured meshes proposed by Balcázar *et al.*[19,16].

Indeed, at the discretized level, $\psi_f = \psi_{C_p} + 0.5\mathrm{L}(\theta_f)(\psi_{D_p} - \psi_{C_p})$[16,19], subindex D_p denotes the downwind point, C_p denotes the upwind point, U_p denotes the far-upwind point, $\psi = \{u_i, \phi\}$, u_i denotes the cartesian components of $\mathbf{v}$, $\beta_f = \{\rho_f, 1\}$, $\mathbf{v}_f$ is interpolated by Eq.(15), $\mathrm{L}(\theta_f)$ is the flux limiter, as defined in[19]. Diffusive terms of transport equations are discretized using a central difference scheme, including non-orthogonal correction (Scheme DS1, Appendix A of[19]). The compressive term in the re-initialization equation (Eq.(7)) can be computed by a central-difference scheme, or equivalently by linear interpolation of the compressive variable ($\phi(1-\phi)$) at the cell-faces, as detailed in Appendix A of[19]. The latter approach is selected in this research. Further technical details as well as an assessment of convective schemes and diffusive schemes on unstructured fixed meshes can be found in[19]. A comparison between different convective schemes using tetrahedral AMR is presented in Section 4.2.1. Gradients, $(\nabla\psi)_P$, are computed at cell centroids by using the least-squares method[16], based on a wide and symmetric stencil that includes the cell-nodes around the vertexes of the current cell Ω_P as proposed in[16], which is weighted by the inverse distance between the current cell-centroid ($\mathbf{x}_P$) and the neighboring points ($\mathbf{x}_i$). The effect of weighting factor in computation of gradients by using the least-squares method is assessed in[20]. In this work, variables at the cell-faces, e.g., $\{\mu_f, \varepsilon_f, \mathbf{n}_f, ...\}$, are linearly interpolated (Eq.(60) Appendix A of[19]), by using a distance-weighted coefficient unless otherwise stated, whereas density at cell-faces (ρ_f) is computed by arithmetic average[16,19]. The fractional step projection method[45,46] is used for solving the pressure-velocity coupling. For present simulations, time integration of predictor step and corrector step is performed by employing a first-order Euler method:

$$\frac{\rho\mathbf{v}^* - \rho^n\mathbf{v}^n}{\Delta t} = \mathbf{A}^n + \mathbf{D}^n + \rho\mathbf{g} + \sigma\kappa\nabla_h(\phi), \tag{12}$$

$$\mathbf{v} = \mathbf{v}^* - \frac{\Delta t}{\rho}\nabla_h(p), \tag{13}$$

where super-index n indicates the previous time step, $\mathbf{v}^*$ is the predicted velocity, $\mathbf{v}$ is the corrected velocity, $\mathbf{A} = -\nabla_h \cdot (\rho\mathbf{v}\mathbf{v})$, and $\mathbf{D} = \nabla_h \cdot (\mu((\nabla_h\mathbf{v}) + (\nabla_h\mathbf{v})^T))$ are explicitly calculated, $(\nabla_h\mathbf{v})^T$ is evaluated by the least-squares method[16].

Coupling the free-divergence velocity constraint with Eq. (13), a Poisson equation for the pressure field is derived,

$$\nabla_h \cdot \left(\frac{1}{\rho}\nabla_h(p)\right) = \frac{1}{\Delta t}\nabla_h \cdot (\mathbf{v}^*), \qquad \mathbf{e}_{\partial\Omega} \cdot \nabla_h p|_{\partial\Omega} = 0. \tag{14}$$

where $\mathbf{e}_{\partial\Omega}$ is a unit normal vector pointing outside the domain surface $\partial\Omega$. The finite-volume discretization of Eq.(14), as detailed in[16], leads to a linear system $\mathbf{Mp} = \mathbf{b}$, which is solved by using a preconditioned conjugate gradient method[47,48]. Indeed, in this work, an equivalent linear system $\mathbf{P}^{-1}\mathbf{Mp} = \mathbf{P}^{-1}\mathbf{b}$ is solved, where $\mathbf{P} = \mathrm{diag}\{\mathbf{M}\}$ is the so-called Jacobi pre-conditioner[48].

In order to satisfy the incompressible constraint (Eq.(2)), and to avoid pressure-velocity decoupling on collocated grids[49,50], a cell face velocity $\mathbf{v}_f$ is defined as follows[13,16]:

$$\mathbf{v}_f = \sum_{q\in\{P,F\}} \frac{1}{2}\left(\mathbf{v}_q + \frac{\Delta t}{\rho_q}(\nabla_h p)_q\right) - \frac{\Delta t}{\rho_f}(\nabla_h p)_f, \tag{15}$$

where P and F are indicating the adjacent cell nodes to the face f. Eq.(15) can be equivalently expressed in terms of the volume flux $\mathbf{v}_f \cdot \mathbf{A}_f$, mass flux $\rho_f\mathbf{v}_f \cdot \mathbf{A}_f$, or normal velocity $\mathbf{v}_f \cdot \mathbf{e}_f$; where $\mathbf{A}_f = \mathbf{e}_f||\mathbf{A}_f||$ is the area vector, and $\mathbf{e}_f$ is a unit normal vector pointing outside the current cell Ω_P[19]. The reader is referred to Appendix B of[13] for additional details on the origin of Eq. (15). The time step Δt, restricted by CFL and stability conditions[43], is given by:

$$\Delta t = C_{\Delta t} min\left(\frac{h}{||\mathbf{v}||}, \frac{\rho h^2}{\mu}, \left(\frac{h}{||\mathbf{g}||}\right)^{1/2}, h^{3/2}\left(\frac{\rho_1 + \rho_2}{4\pi\sigma}\right)^{1/2}\right), \tag{16}$$

where $C_{\Delta t} = 0.1$ for the current method and h is defined as the characteristic size of the control volume P, which is calculated as an average of the distances between the centroid of P and the neighbor cells centroids, unless otherwise stated. Finally, a TVD Runge-Kutta method[51] is employed for time integration of advection Eq.(6) and re-initialization Eq.(7). The re-initialization Eq.(7) time step is restricted by its viscous term as follows $\Delta\tau = C_\tau min\{(h^2)/\varepsilon\}$, where C_τ is taken to be ~ 0.05[16,19]. In present simulations, one iteration of the re-initialization equation (Eq.(7)) per physical time-step is enough to keep the CLS profile.

The numerical algorithms have been implemented in a parallel C++/MPI platform called TermoFluids[52]. Furthermore, the unstructured finite-volume CLS method has been extensively verified and validated with several results from the literature, including dam-break[16], rising bubbles[16,21,53,54], bubbly flows[17,18,19], droplet collision against a fluid-fluid interface and droplets bouncing collision[18], thermocapillary-driven motion of deformable fluid particles[13], Taylor bubbles[55], atomization of a liquid-gas jet[56,57], non-Newtonian two-phase flow[58], and mass transfer from bubble swarms[19,20]. Therefore, this research can be considered as a further step in the development of numerical methodologies to solve two-phase flows on complex geometries,

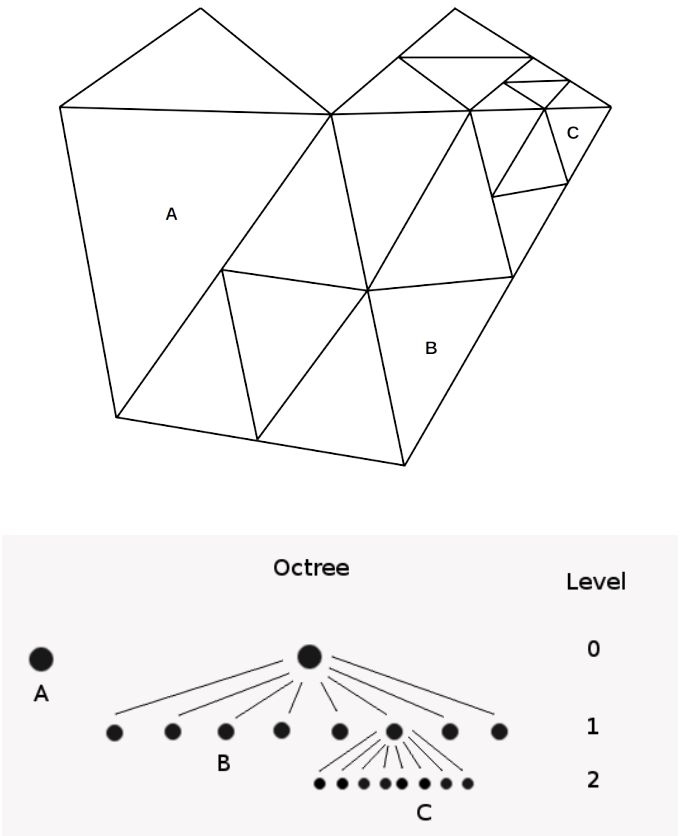

FIGURE 1 Illustration of the regular refinement and octree data structure for 3D tetrahedral meshes

with the aid of a finite-volume/level-set method introduced by [19,17,13,16], and an adaptive tetrahedral-mesh refinement method proposed in this work.

3 | ADAPTIVE MESH REFINEMENT FOR TETRAHEDRAL MESHES

The present computational approach uses an adaptive mesh refinement algorithm based on an octree data structure and regular refinement for 3D tetrahedral meshes (See figure 1). This method generates a unit mesh according to a prescribed physics-based criterion. The newly adapted mesh is obtained from an input mesh through some geometrical manipulations: operations of refinement and coarsening until a maximum level of refinement is achieved. This methodology is a further step to extend our previous work about the development of AMR algorithms on hexahedral meshes [59,56,57,54,60] to tetrahedral meshes for the solution of computational fluid dynamics problems on complex domains.

3.1 | Mesh definition and domain decomposition

For the AMR method described here, we will shortly explain the primary inputs that we need to execute our algorithm and how it is implemented on our multi-physics unstructured CFD code. The mesh used for numerical simulation is based on three main elements: vertex, faces, and cells. Each of these items keeps a local and global identification number (id). For example, element cell keeps the information related to the id of its faces and vertex; element face stores the id of its vertices and the id of the cells that are sharing this face, and element vertex stores the spatial coordinates.

With this mesh representation, the non-conformed elements are allowed in our unstructured CFD code. In the present AMR method, the transition cells that appear between refinement levels will create a tetrahedral cell with more faces and vertices than

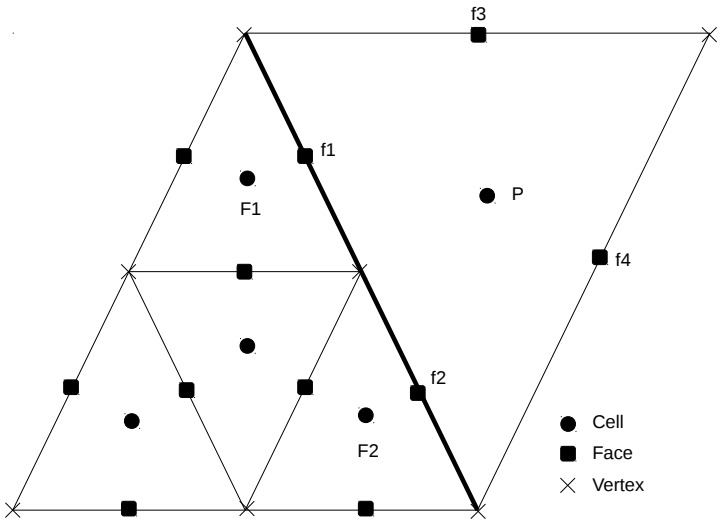

FIGURE 2 Illustration of the 2D planar representation of non-conformed elements

a regular one (see Figure 2). Our unstructured CFD code will represent this cell as a polyhedron, and the numerical schemes described in Section 2.3 allow the use of this element.

3.2 | Algorithm description and parallelization strategy

The tetrahedral AMR is added in the global algorithm for the unstructured CLS method[16], and the tetrahedral AMR loop is reinitialized when the bubble centroid has advanced a distance equal to the minimum grid size of the computational domain Ω. The global tetrahedral AMR-CLS algorithm follows the next steps:

1. Compute the minimum grid size h_{min} in Ω and the initial position of the bubble centroid b_{co}.
2. Compute Δt by Eq. (16).
3. Solve level-set advection Eq. (6) and re-initialization Eq. (7).
4. Physical properties (ρ, μ) are updated according to Section 2.2
5. Compute $\mathbf{v}^*$, p, $\mathbf{v}$ and $\mathbf{v}_f$ by the fractional-step method as in Section 2.3: Eq.(12) → Eq.(14) → Eq.(13) → Eq.(15).
6. Compute the actual bubble centroid position b_c.
7. **if** $(||b_c - b_{co}|| < h_{min})$ Repeat steps 2-5.
   else Re-mesh and repeat steps 1-6 until the desired time is reached.

The Re-mesh step consists on the physics-based criterion calculation, generation of adapted meshes and solution interpolation, described as follows:

- Physics-based criterion calculation. The level-set function ϕ is employed to distinguish the interface between fluids, and locally refine the mesh when $0 + \epsilon < \phi < 1 - \epsilon$, where $\epsilon = 1e - 4$. Moreover, to avoid the refinement process to be often repeated, up to three layers of neighboring cells close to the fluid interface will be refined. This procedure is done to ensure a good mesh resolution for the interface when it moves in any spatial direction.

- Generation of adapted meshes. At each Re-mesh step, the current mesh and the corresponding physical criterion is processed to create the newly mesh. The refinement step is based on an 8-subdivision procedure for tetrahedron elements (See Fig.

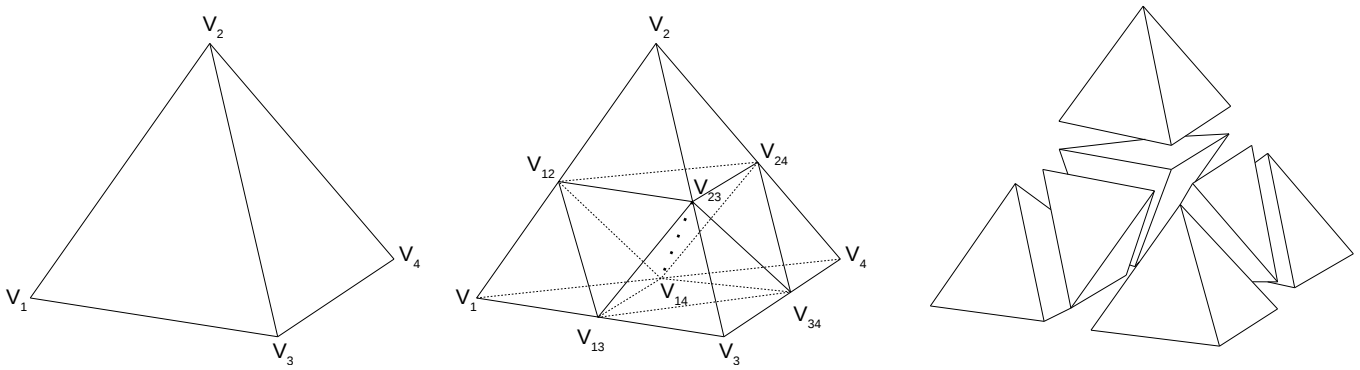

FIGURE 3 Illustration of the regular refinement of a tetrahedron

3). The coarse mesh is refined to the level of resolution needed for the simulation. Moreover, a geometrical criterion is taken into account at the moment of the subdivision, diminishing the drop on the quality metric from the original cell to its children cells. The parallel algorithm for the subdivision procedure of a coarse partitioned mesh follows the next steps, where each one of them are executed independently on every grid subdomain with fixed interfaces:

1. Read mesh to be refined
2. Create a new mesh object and insert the vertex needed from the coarse mesh.
3. New vertex will be created on the edges of the elements. Thus, an edge data structure is used to create new vertex without duplicate them on the subdomain boundaries.
4. Unique global indexes are assigned according to the old indexes from the parent element to be subdivided.
5. Create new faces and cells according to a criterion to preserve the quality of the coarse mesh.
6. Parallel creation of an HDF5 data file with new mesh.

For step 3 and 4, cells elements can be created uniquely, without duplication on each parallel subdomain, but faces and vertex need special treatment. For the faces that are shared between two parallel subdomains, the global identification number is just assigned by the subdomain with the lowest rank and copied to the highest rank. In the case of the vertex elements, that are shared among many ranks, a master-slave procedure is followed. As indicated in Fig. 4, the edge data structure is sent by each slave-rank to the master-rank. Here, the master-rank compares the edge information from each slave-rank to avoid duplication of new mesh elements and establishes a unique global index for the new vertex. Then, the proper information about indexes is sent back to the slaves-ranks to complete the new mesh. The quality of the refined mesh is important to get good numerical approximations and results. On the subdivision of tetrahedron cells on step 5, a criterion is followed to ensure that the quality of the new tetrahedron will have similar quality as the parent cell. This criterion consists of the inner edge of a tetrahedral has to connect its longest edges to generate eight tetrahedrons that will be similar to the original tetrahedron[41]. This can be shown in the Figure 3, where the edge $\overline{V_{23}V_{14}}$ was the one chosen between the possible edges $\overline{V_{23}V_{14}}$,$\overline{V_{13}V_{24}}$ and $\overline{V_{12}V_{34}}$, according to the criterion. Moreover, at each level of refinement, the new mesh is partitioned using the ParMETIS library[61] to ensure a good load balance for its use on parallel computing simulations. (See Fig. 5).

- Solution interpolation. Between time intervals, the solution has to be transferred from one mesh to the newly. For now, we use a hierarchical cell evaluation mechanism: given any cell in the domain, it provides the value at this point and its hierarchical position on the octree data structure. Then, an average process is performed for the coarsening, and a pass value is done for the refinement process in the computational space.

The multiphase solver[16,17,19] was designed for general unstructured meshes. Indeed, Eq.(15) applies also to adjacent cells at a different level, taking into account that this is a particular case of unstructured arrange. The face velocity (Eq.(15)) can also be expressed, for instance, in terms of the volumetric flux (see Appendix B of[13]). It means that the sum of the volumetric fluxes around the cell keeps conservative after the re-meshing process.

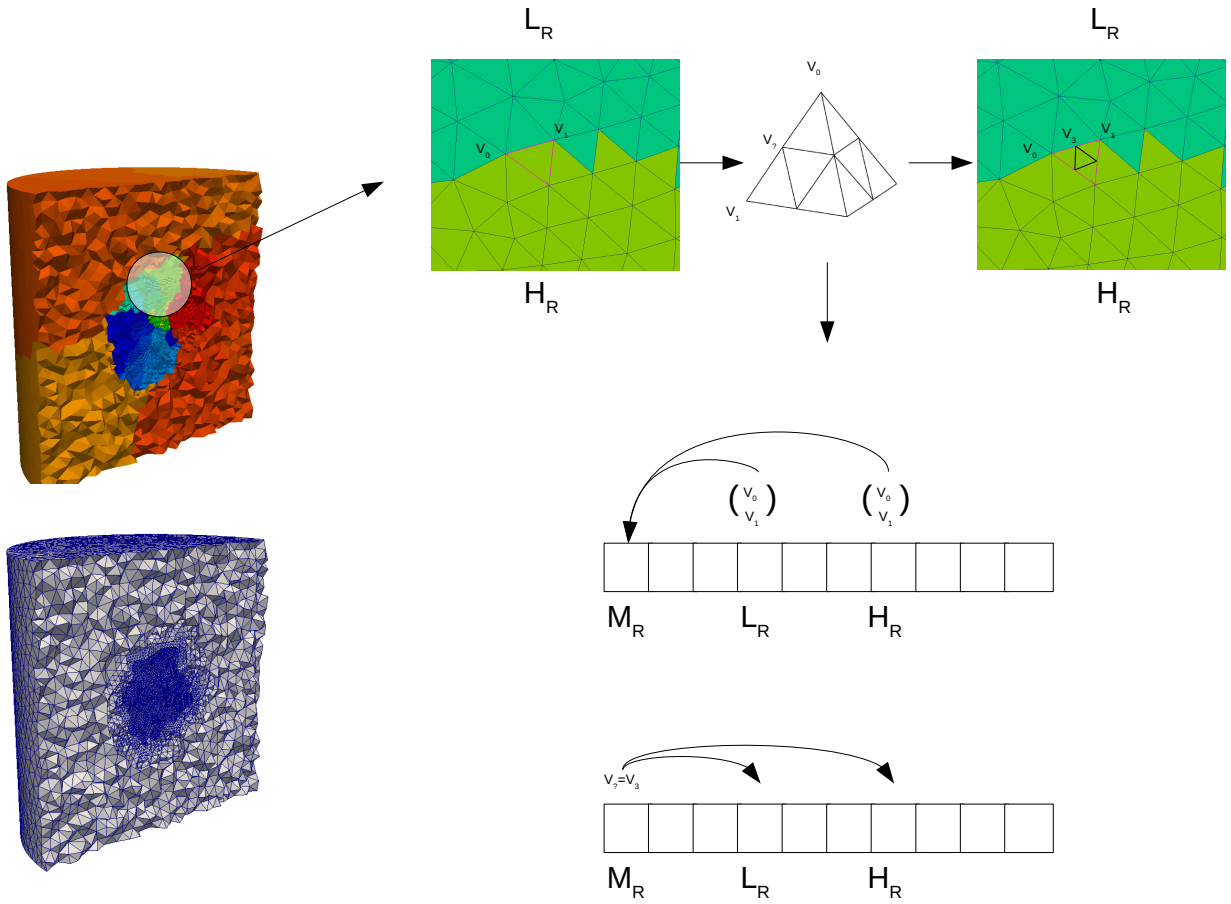

FIGURE 4 Illustration of global Id assignment for a new vertex, shared between processors. L_R =Lowest rank; H_R =Highest rank; M_R =Master rank

The code has been executed on the supercomputers MareNostrum IV and Altamira using up to 144 cores for 3D simulations of gravity-driven bubbles/droplets. Moreover, the parallel performance for the steps explained in the generation of adapted meshes has been executed up to 384 CPU-cores showing a good strong speed up for the AMR of a tetrahedral mesh where the size to be refined was one million tetrahedron cells. This test has been performed in the supercomputer MareNostrum IV. In Figure 6, is shown the strong speedup for the AMR mesh algorithm, where up to 192 CPU-cores it reaches an efficiency close to 90%

4 | NUMERICAL EXPERIMENTS

In this section, numerical tests for validation are described, and new numerical experiments related to gravity-driven bubbles/-droplets in regular and complex domains are analyzed. The dimensionless numbers governing gravity-driven flows[62,63] are the Eötvös number (Eo), Morton number (M), Reynolds number (Re), and the ratios of physical properties (density ratio η_ρ and viscosity ratio η_μ), defined as follows

$$Eo = \frac{gd^2\Delta\rho}{\sigma}, \qquad M = \frac{g\mu_1^4\Delta\rho}{\rho_1^2\sigma^3}, \qquad Re = \frac{\rho_1 U_T d}{\mu_1}, \qquad \eta_\rho = \frac{\rho_1}{\rho_2}, \qquad \eta_\mu = \frac{\mu_1}{\mu_2}, \tag{17}$$

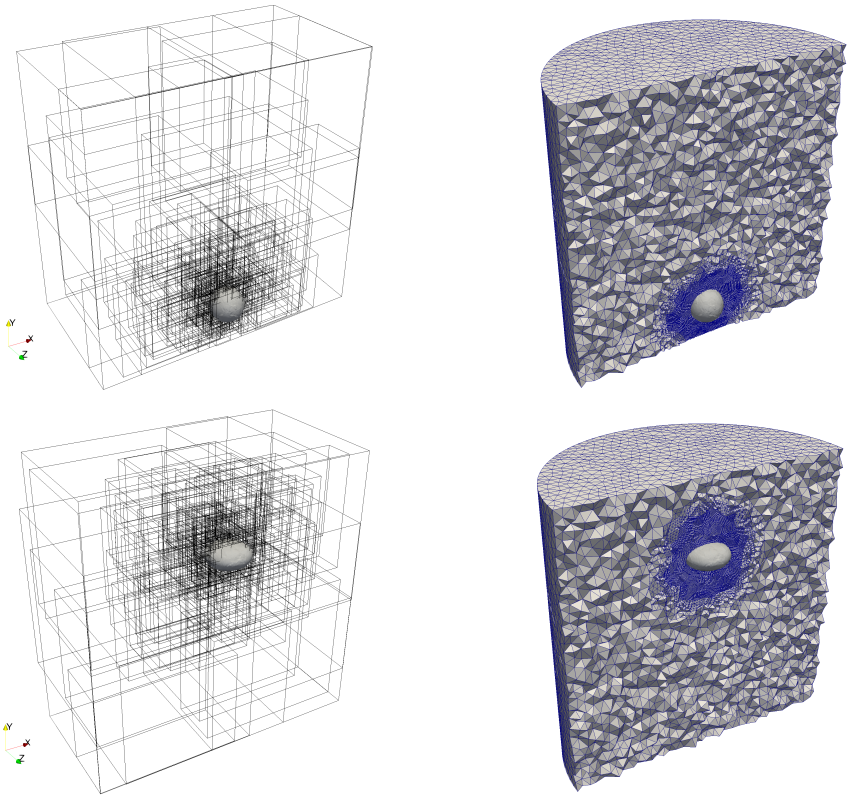

FIGURE 5 Parallel partition and the computational grid for the AMR mesh of gravity-driven bubble simulation at different adaptation times

where subindex 1 refers to the continuous fluid phase, subindex 2 refers to the fluid inside the bubble, d is bubble diameter and $\Delta\rho = \rho_1 - \rho_2$ is the density difference between fluids. The terminal bubble velocity is computed by,

$$U_T = \frac{\int_{\Omega_2} v_y dV}{\int_{\Omega_2} dV}, \tag{18}$$

and dimensionless time is defined as, $t^* = t\sqrt{g/d}$. Furthermore, the grid resolution is established as $h = V_{tet}^{1/3}$, where V_{tet} is the tetrahedron volume, and sphericity (bubble shape) is defined as

$$\zeta = \frac{\pi d^2}{\int_\Omega ||\nabla\phi|| dV}. \tag{19}$$

4.1 | Advection test

A three-dimensional advection test is presented to assess the method with different grid sizes. A sphere with $d = 0.25$ is located at $(L/2; (L/2) + d; L/2)$ in a cubic domain of dimensions $[(0, L)^3]$ with $L = 2$. A velocity field is kept constant in time and is defined as follows, $\mathbf{v}_x = y - L/2$, $\mathbf{v}_y = x - L/2$ and $\mathbf{v}_z = 0$ where x, y and z are the spatial coordinates. Figure 7 shows a time sequence of the sphere following the rotational velocity field and the corresponding AMR grid with three levels of refinement.

For this test, three different grid sizes $h = (d/30; d/40; d/50)$ have been considered to show the accuracy of the method. Results of the time evolution for the mass conservation error and sphericity with different grid sizes are shown in figure 8, where the mass conservation error is calculated by

$$M_r = [M(t) - M(0)]/M(0), \tag{20}$$

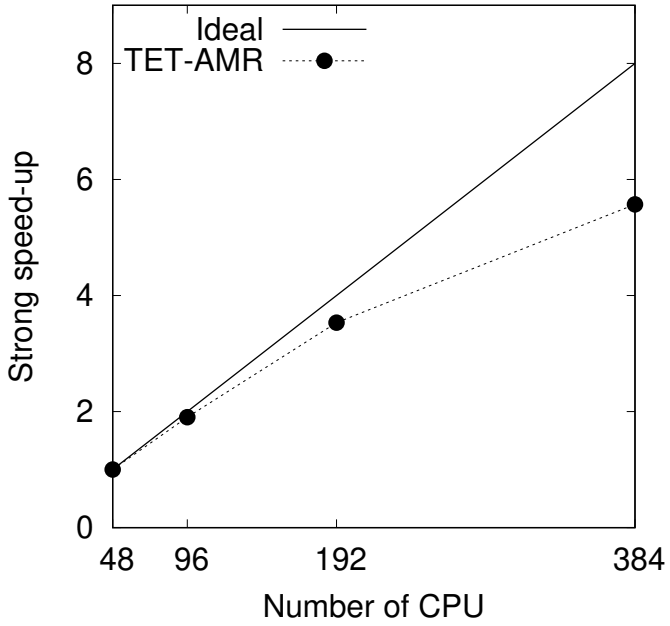

FIGURE 6 Strong speed up for tetrahedral AMR algorithm, where one million tetrahedron cells are 8-subdivided

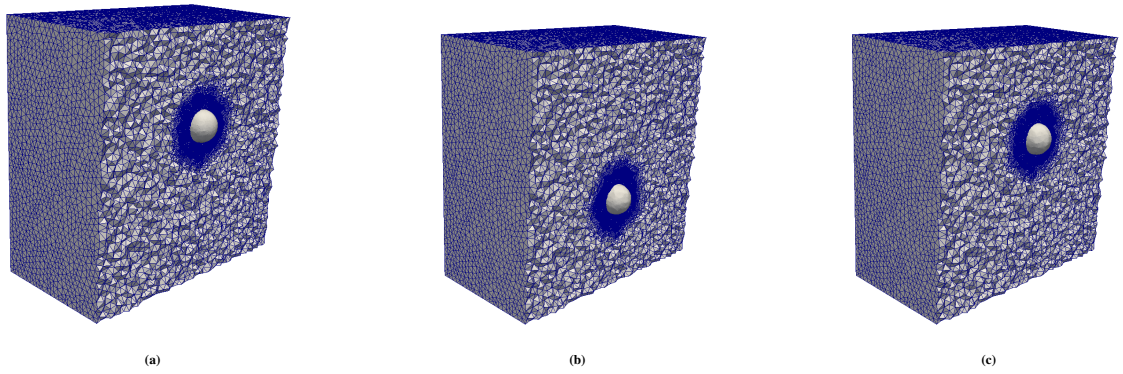

FIGURE 7 Bubble shape and its respective 3D AMR grid for the advection test at different times. (a) t=0, (b) t=3.14, (c) t=6.28

$$M(t) = \int_{\Omega} \phi dV. \tag{21}$$

It can be noticed that the mass conservation is well kept for different grid sizes and sphericity tends to unity when the grid size is reduced.

Furthermore, in figure 9, the initial sphere is compared with its final shape after one rotation around the center of the domain with the finest grid resolution. As it is shown, the method is capable of keeping a correct spherical shape with an tetrahedral AMR.

4.2 | Three-dimensional buoyant bubble in a cylindrical domain

In this section, the methodology is validated with the rising bubble of an ellipsoidal bubble in a quiescent liquid. The dimensionless numbers selected are depicted in Table 1.

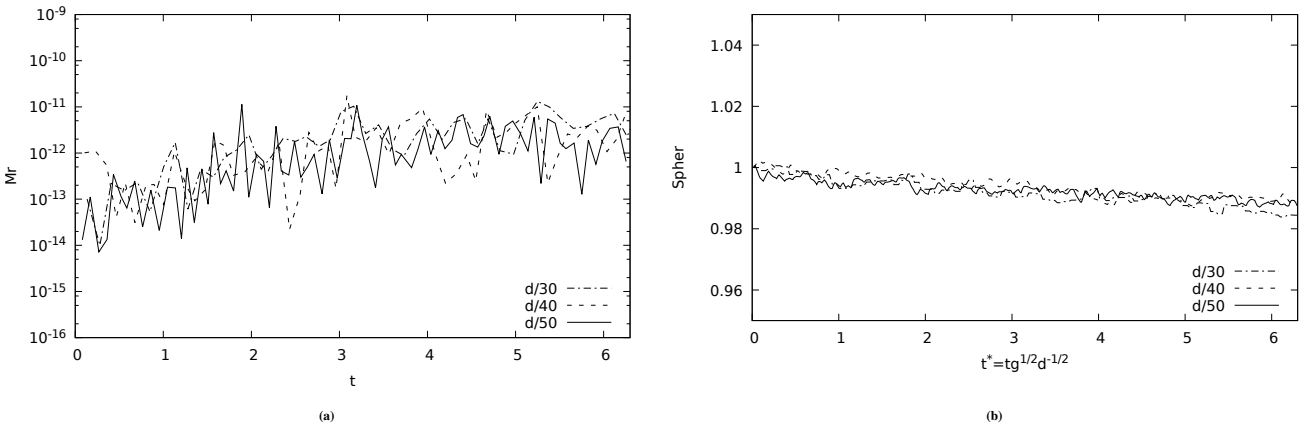

FIGURE 8 Time evolution of the (a) mass conservation error and (b) sphericity for different grid resolutions.

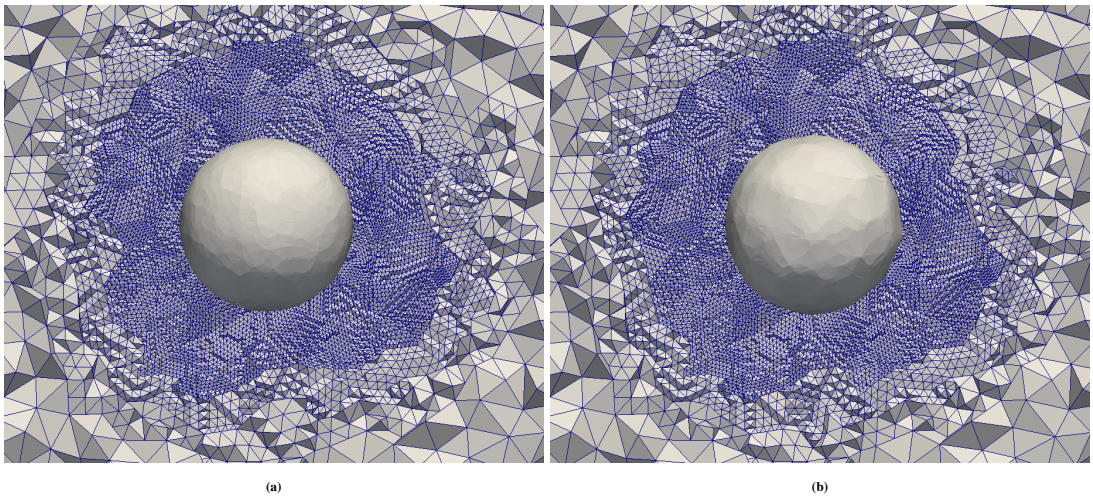

FIGURE 9 Close-up to the bubble shape and AMR grid ($h = d/50$) for the (a) initial state and (b) after an entire lap.

Eo	$logM$	ρ_1/ρ_2	μ_1/μ_2
4.88	−4.9	100	100

TABLE 1 Dimensionless numbers for the presented test.

The dimensions of the cylindrical domain are the following: $D_{cyl} = 8d$ and $H_{cyl} = 8d$, where the initial bubble of diameter $d = 0.25$ is located at $(x, y, z) = (0, d, 0)$. Moreover, the boundary conditions in the top/bottom walls are no-slip, whereas the Neumann condition is applied on the lateral walls. The initial mesh is around 54k control volumes, and AMR was used to achieve the desired grid resolution in the interface and the near wake (See Fig. 10). The final number of control volumes is presented in Table 2.

The final bubble shape is consistent with the experimental result of[64], where the bubble reached an ellipsoidal shape (see Figure 11). Moreover, in Figure 12a, the terminal Reynolds number is shown for different grid resolutions.

Fig. 12b reports the order of convergence (p) for the method, which is second order (p≈2), where the L_1 norm was measured as $L_1 = (Re(ref) - Re(h))/Re(ref)$, and the solution with the finest grid ($h = d/40$) was taken as $Re(ref)$. Additionally, the effect of different density/viscosity ratios have been plotted in figure 12c, where the Re number is shown using the finest grid

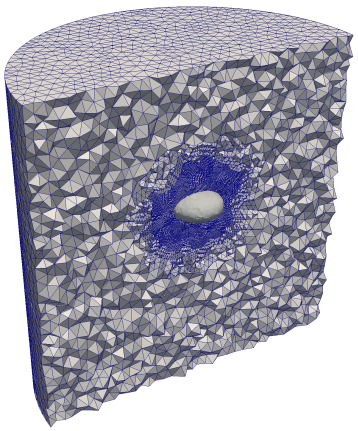

FIGURE 10 AMR for the test case $Eo = 4.88$, $logM = -4.9$, with a grid resolution of 40 control volumes per diameter at the interface.

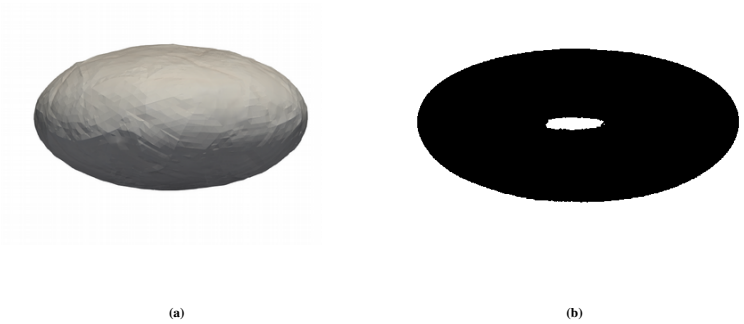

FIGURE 11 (a) Bubble shape for $Eo = 4.88$, $logM = -4.9$. (b) Experimental bubble shape by[64].

($h = d/40$). The results of these simulations presented a similar outcome when the ratio was increased from 50 to 1000, but for better computational performance and accuracy the ratio 100 was established for the simulations presented in this paper.

The bubble aspect ratio measured in the experiments by[64] is defined by

$$E = \frac{shortest \quad radius}{longest \quad radius}, \tag{22}$$

The computed Reynolds number and the bubble aspect ratio are compared to experiments reported by[64] (See Table 2). As it can be shown, our present results are in good agreement with the experimental data.

Case $Eo = 4.88$, $logM = -4.9$	Number of control volumes	Re	E
[64]		51.7	0.49
Present AMR-CLS ($h = d/25$)	7.00e+05	51.90	0.54
Present AMR-CLS ($h = d/30$)	9.00e+05	52.23	0.54
Present AMR-CLS ($h = d/35$)	1.30e+06	52.46	0.53
Present AMR-CLS ($h = d/40$)	2.00e+06	53.00	0.53

TABLE 2 Present Re computations compared with experimental results by[64].

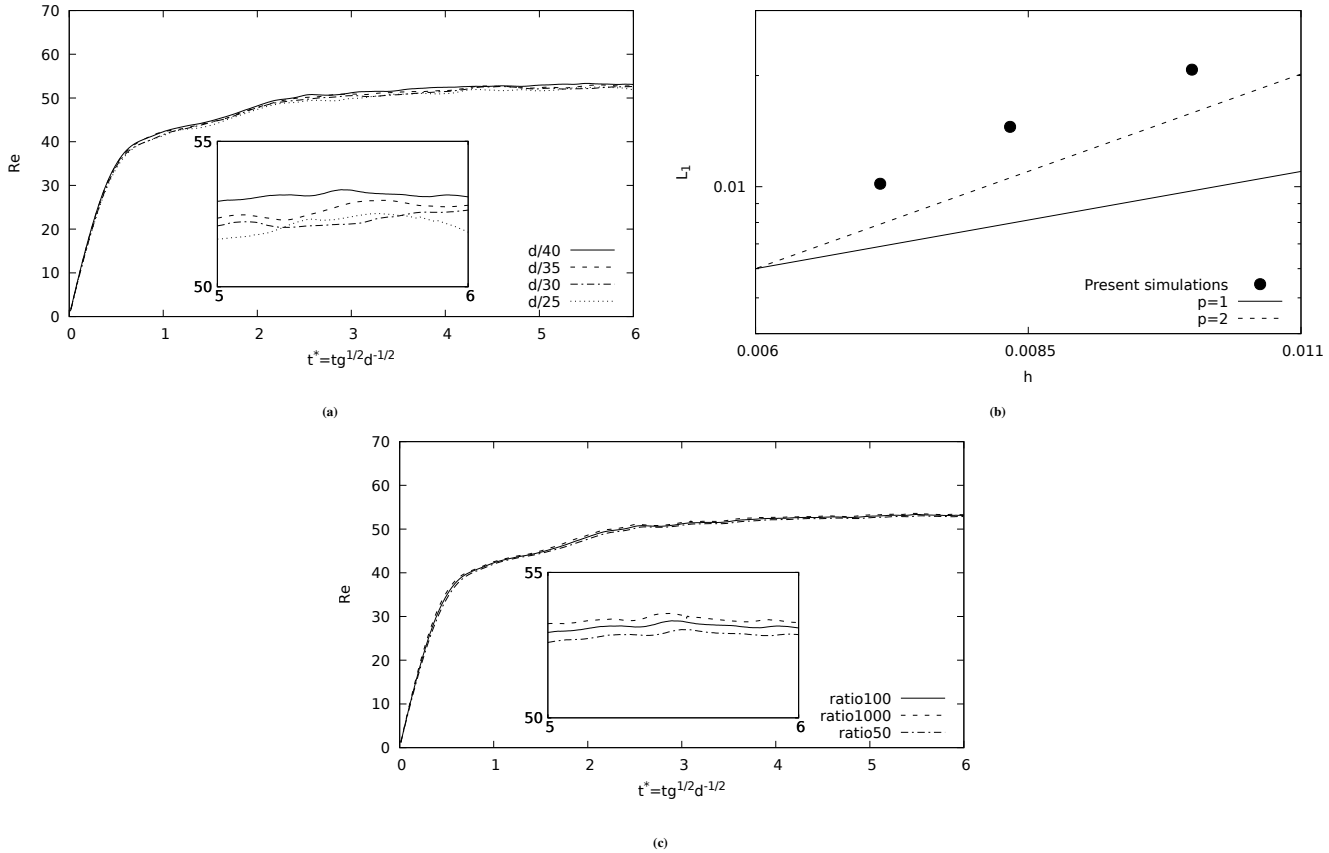

FIGURE 12 Gravity-driven bubble in an infinite domain for $Eo = 4.88$, $logM = -4.9$ (a) Grid convergence; (b) Order of convergence for the method measured by L_1 norm; (c) Effect of using different density and viscosity ratios.

4.2.1 | Comparison of different convective schemes

The convective term discretization of Eq. (1) is based on unstructured flux-limiters schemes proposed by [19,16]. Here, $L(\theta_f)$ denotes the flux-limiter, θ_f is the upwind ratio of consecutive gradients of the velocity components, as defined in Appendix A of [19]. The flux-limiters employed in this assessment are summarized in Table 3, which includes Central Difference (CD), Upwind, Superbee and SMART limiters [65,66,67]. The reader is referred to [19,16] for more details about the unstructured flux-limiters based convective schemes, used in this research.

	$L(\theta_f)$
Central difference limiter (CD)	1
TVD Superbee limiter [65]	$max(0, min(2\theta_f, 1), min(2, \theta_f))$
SMART limiter [66,67]	$max(0, min(4\theta_f, 0.75 + 0.25\theta_f, 2))$
First-order upwind limiter	0

TABLE 3 Flux limiters $L(\theta_f)$ used in this work.

In Figure 13a, the Central Difference, Upwind, Smart, and Superbee schemes are compared to the solution of terminal Reynolds number for the case with $Eo = 4.88$, $logM = -4.9$, with the same properties as in Section 4.2, but with a grid resolution of $d/40$. As can be seen, the use of different flux limiters leads to similar results for terminal Reynolds number and Superbee scheme will be selected for the next test cases, as it prevents numerical oscillations at discontinuities and minimizes

numerical diffusion. Furthermore, CLS-AMR shows excellent mass conservation (see Fig. 13b), where the mass conservation error is calculated by Eqs. 20 and 21.

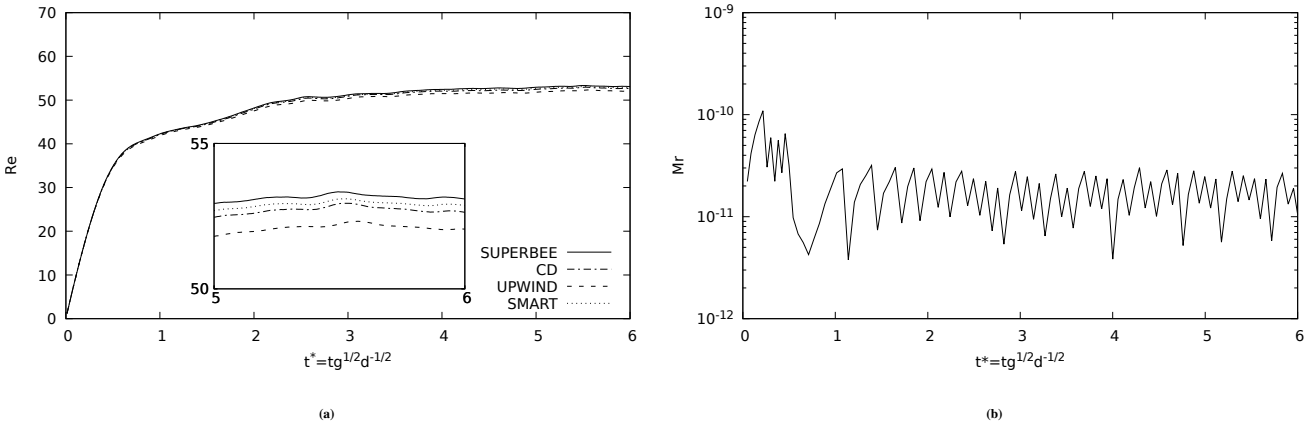

FIGURE 13 Gravity-driven bubble in an infinite domain for $Eo = 4.88$, $logM = -4.9$ (a) Effect of the convective scheme used to discretize the momentum Eq. (1); (b) Mass conservation error using the finest grid and TVD Superbee flux limiter.

4.2.2 | Mesh compression, quality and CPU time

The dynamic mesh adaptation, up to three levels of refinement, increased the initial number of control volumes from $54k$ to near $2M$. Temporal evolution of the total number of control volumes for this case with $Eo = 4.88$, $logM = -4.9$ is depicted in figure 14a. As it can be seen, the number of control volumes is very stable for the entire simulation. It is important to point out that the equivalent fixed mesh, with a grid resolution close to three levels of refinement, will contain near 27M of control volumes, which makes a compression rate equal to 93%.

In section 3.2, a criterion to preserve the quality of the mesh is followed. A quality metric is calculated for each tetrahedron, to evaluate the mesh quality, given by

$$\eta = 12(3v)^{(2/3)} / \sum_{0 \le i < j \le 3}^{n} l_{ij}^2, \tag{23}$$

where v is the volume of the tetrahedron, and l_{ij} are the lengths of the tetrahedron edges. Equation 23 is the tetrahedron shape measure that is equivalent to two commonly shape measures: minimum solid angle and radius ratio (from 0, worst, to 1, best) (see[41]). In figure 14b, the temporal evolution of the minimum, maximum and an average over the entire mesh of the quality metric is presented. It is shown that during the entire simulation the quality is mostly preserved and there are no significant changes.

For time testing purposes, an unstructured fixed mesh was created for the case $Eo = 4.88$, $logM = -4.9$. The fixed mesh contained a significant density of control volumes near the center of the domain, where the bubble will follow its path (approximately 9M control volumes), reaching a minimum grid size similar to an adaptive mesh with three levels of refinement. The CPU time for the fixed mesh and the adaptive mesh are displayed in Table 4. The simulations were done with 144 cores in the Altamira supercomputer. These results show the time to run until $t^* = 2.07$, including adaptation times, and reaching a similar state. From this information, it shows that the simulation time of the adaptive mesh is far less compared with the fixed mesh, and as shown in figure 14c, the difference in the computed Re number between the fixed and tetrahedral AMR mesh is insignificant.

4.3 | Three-dimensional drops in vertical pipes

In this section, the methodology is validated with the rising of different drops in a vertical pipe and the effect of the wall and the diameter ratio λ on the rising motion are researched. Here, additional dimensionless numbers are introduced as $Eo_D = (gD^2\Delta\rho)/(\sigma)$, and $\lambda = d/D$, where D is the pipe diameter and d the drop diameter. The dimensionless numbers selected are depicted in Table 5.

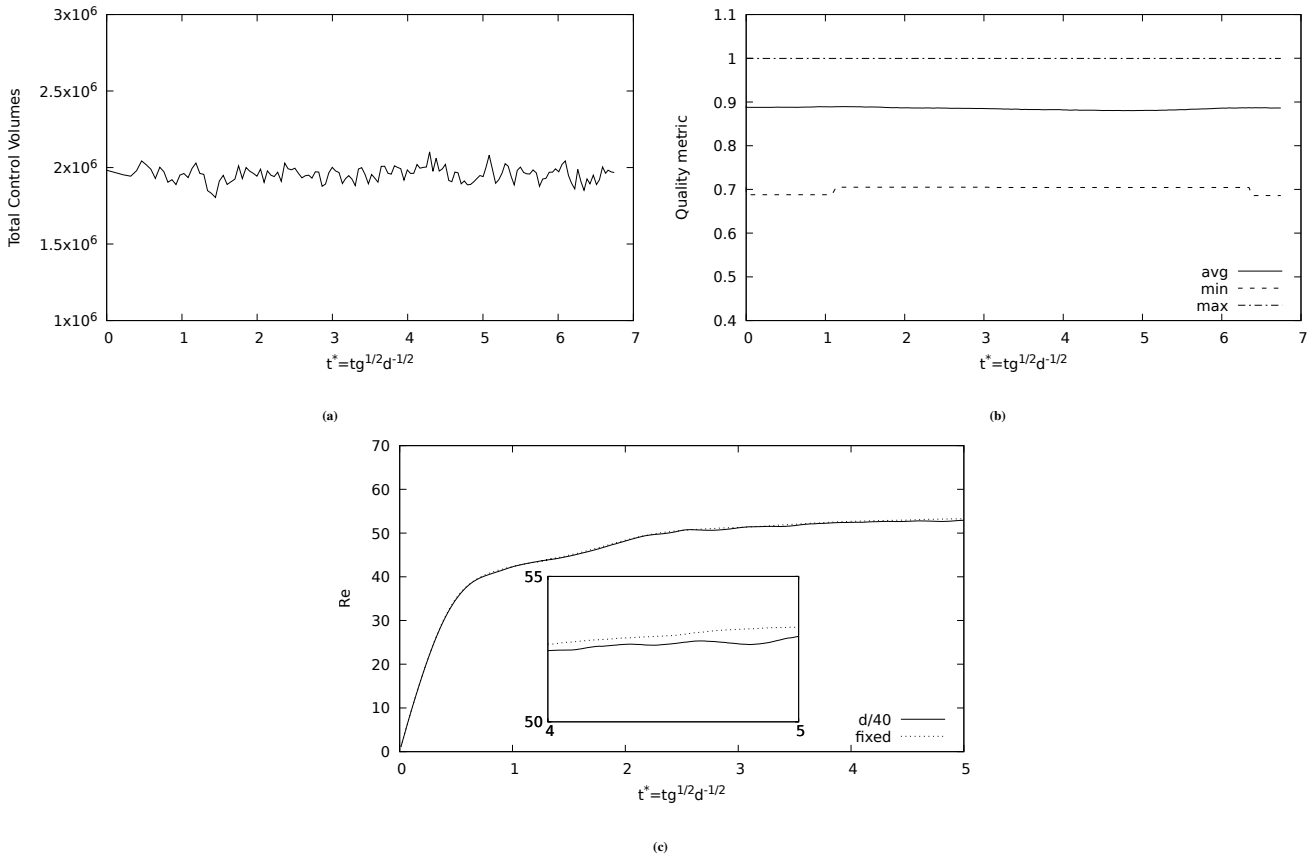

FIGURE 14 Gravity-driven bubble in an infinite domain for $Eo = 4.88$, $logM = -4.9$ (a) Temporal evolution of the total number of control volumes; (b) Temporal evolution of the quality metric defined by Eq. (23); (c) Comparison of the temporal evolution of Re number between a fixed and tetrahedral AMR mesh both with $h = d/40$.

Mesh	Level of refinement	$t^* = t\sqrt{g/d}$	$CPU\ Time(h)$
Fixed	0	2.07	104.17
Adaptive mesh	3	2.07	32.87

TABLE 4 Computational times for fixed and tetrahedral adaptive mesh for gravity-driven bubble $Eo = 4.88$, $logM = -4.9$, using 144 cores in Altamira supercomputer.

The dimensions of the cylindrical domain Ω are the following: $D = 0.5$ and $H = 7.0^* D$. For the case A and B, the initial drop of diameter $d = \lambda^* D$ is located at $(x, y, z) = (0, d, 0)$. For the case C, an initial condition consisting in a cylinder with an equivalent volume to an sphere with $d = \lambda^* D$ was located at $(x, y, z) = (0, d, 0)$. Moreover, the boundary conditions in the top/bottom walls are Neumann conditions, whereas the no-slip condition is applied on the lateral walls. The initial mesh is around 27k control volumes, and AMR was used to achieve the desired grid resolution ($h = D/120$) in the interface and the near wake (See Fig. 15). The approximate final number of control volumes are presented in Table 6.

The computed Reynolds number and drop shapes are compared to experiments and correlation reported by[68] (See Table 6 and Figures 15,16). As it can be shown, our present results are consistent with the experimental and calculated results of[68]. Moreover, as the diameter ratio is increased, the shapes go from a deformed spheroidal to a Taylor drop with bullet shape. For the case C, the Taylor drop gets a spheroidal shape at the nose and is flat at the rear. Here, these test cases illustrate the importance of the diameter ratio λ, as a parameter that control the drop shape and velocity, where a drop will turn into a bullet shape when it has overpassed a critical value, as it has been explained by[68].

$Case$	Eo_D	$logM$	ρ_1/ρ_2	μ_1/μ_2	λ
A	31.0	−4.8	1.245	0.8620	0.30
B	31.0	−4.8	1.245	0.8620	0.54
C	31.0	−4.8	1.245	0.8620	1.23

TABLE 5 Dimensionless numbers for the presented tests.

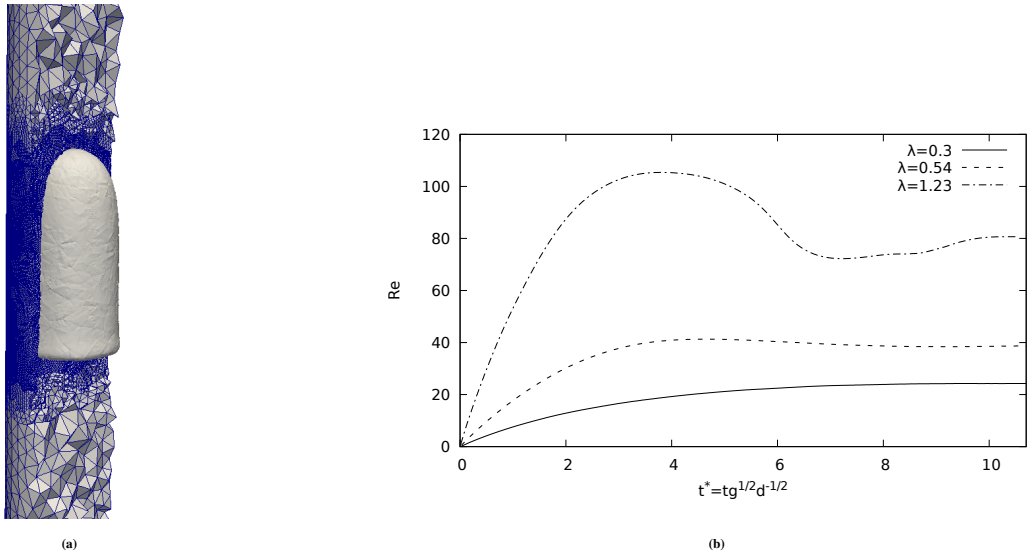

FIGURE 15 (a) AMR for the test case $Eo_D = 31.0$, $logM = -4.8$, $\lambda = 1.23$, with an effective grid resolution of 120 control volumes per tube diameter at the interface. (b) Terminal Re number for $Eo_D = 31.0$, $logM = -4.8$ with different λ

Case	Number of control volumes	Re_{exp}	Re_{cal}	Re
A	7.00e+05	24.26	21.84	24.77
B	1.80e+06	36.90	40.47	38.95
C	3.20e+06	74.95	67.44	80.62

TABLE 6 Present Re computations compared with experimental Re_{exp} by [68] and calculated Re_{cal} by [68].

4.4 | Three-dimensional buoyant bubble in a vertical pipe

In this section, the density and viscosity ratios are increased and the methodology is validated with the rising of a bubble in a vertical pipe and the effect of the wall on the rising motion is researched. The dimensionless numbers selected for the first test are depicted in Table 7.

Eo	$logM$	ρ_1/ρ_2	μ_1/μ_2	λ
3.00	−6.0	100	100	0.5

TABLE 7 Dimensionless numbers for the first presented test.

The dimensions of the cylindrical domain Ω are the following: $D_{cyl} = 2d$ and $H_{cyl} = 14d$, whereas the diameter ratio $\lambda = d/D_{cyl} = 0.5$. The initial bubble of diameter $d = 0.25$ is located at $(x, y, z) = (0, d, 0)$. Moreover, the boundary conditions in the top/bottom walls are Neumann conditions, whereas the no-slip condition is applied on the lateral walls. The initial mesh is

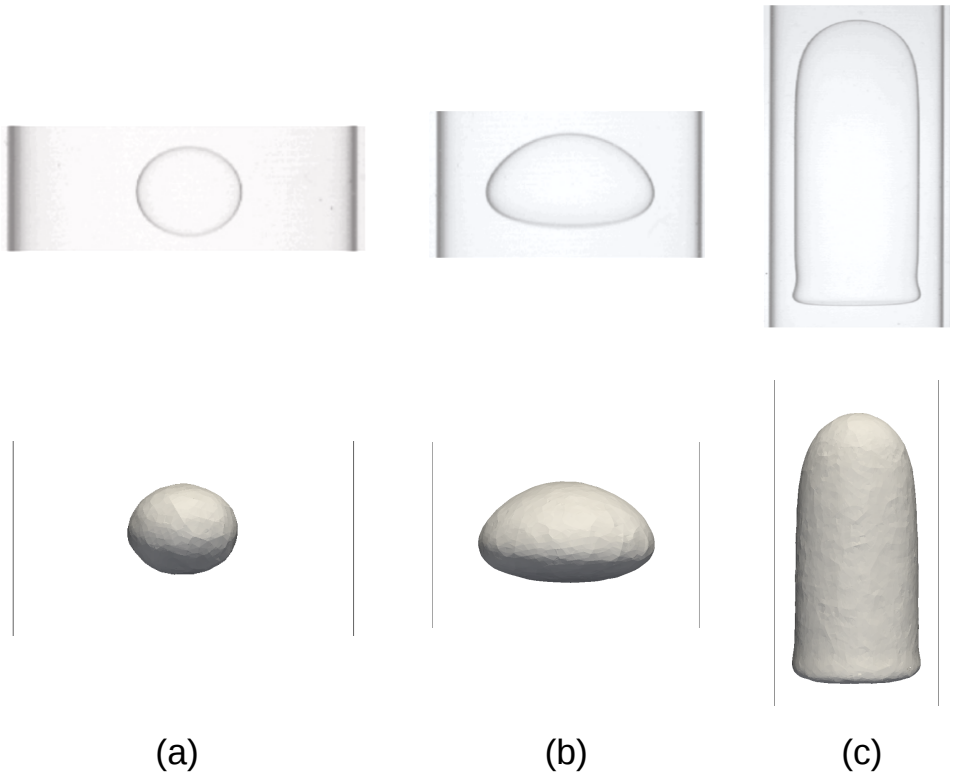

FIGURE 16 Experimental image[68] (top) and present computation (bottom) for bubble shape with $Eo_D = 31.0$, $logM = -4.8$ (a) $\lambda = 0.30$, (b) $\lambda = 0.54$, (c) $\lambda = 1.23$.

Case $Eo = 3.0$, $logM = -6$	Number of control volumes	Re
[63] Infinite domain		85
[17] DNS	9.00e+05	57
Present AMR-CLS ($h = d/60$)	1.60e+06	56

TABLE 8 Present Re computations compared with experimental results (infinite domain) by[63], and numerical results by[17].

around 27k control volumes, and AMR was used to achieve the desired grid resolution ($h = D_{cyl}/120$) in the interface, nearby the walls and in the near wake (See Fig. 17). The final number of control volumes is presented in Table 8.

Figure 18a shows the time evolution for the Reynolds number and the bubble shape. The observed Re is lower compared to the experimental Reynolds for an infinite domain, due to the increase of the drag force when the bubble is very close to the walls. Moreover, the bubble shape reaches a consistent ellipsoidal shape, and its motion is aligned with the symmetry axis of the computational domain.

The computed Reynolds number is compared to experiments, for infinite domain, reported by[63] and numerical results in a confined domain presented by[17](See Table 8). The scale factor relation SF, suggested by[62], is a velocity relation given for the influence of the wall on the single bubble rise velocity, which is defined by

$$SF = U_T/U_{T_\infty} \tag{24}$$

For this case, with $d/D_{cyl} = 0.5$, and according to Eq. (24), the present numerical result is $SF_{num} = 0.66$, which agrees well with the value given by[62] with $SF = 0.64$. In Figure 17, the vorticity field is shown and presents the formation of a double vortex at the bottom of the bubble with the opposite direction. Moreover, the presence of counter-rotating vortices at the walls, which increases the total drag, are shown. This phenomenon leads to achieve terminal conditions within a short distance of the bubble release.

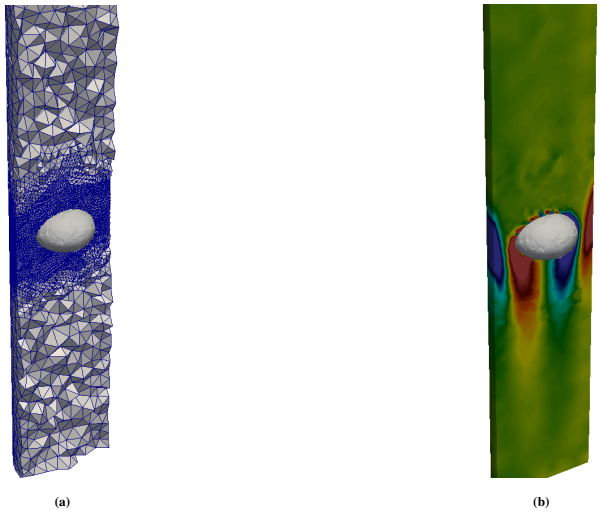

FIGURE 17 (a) AMR for the test case $Eo = 3.0$, $logM = -6.0$, with an effective grid resolution of 120 control volumes per pipe diameter at the interface. (b) Vorticity field for $Eo = 3.0$, $logM = -6.0$.

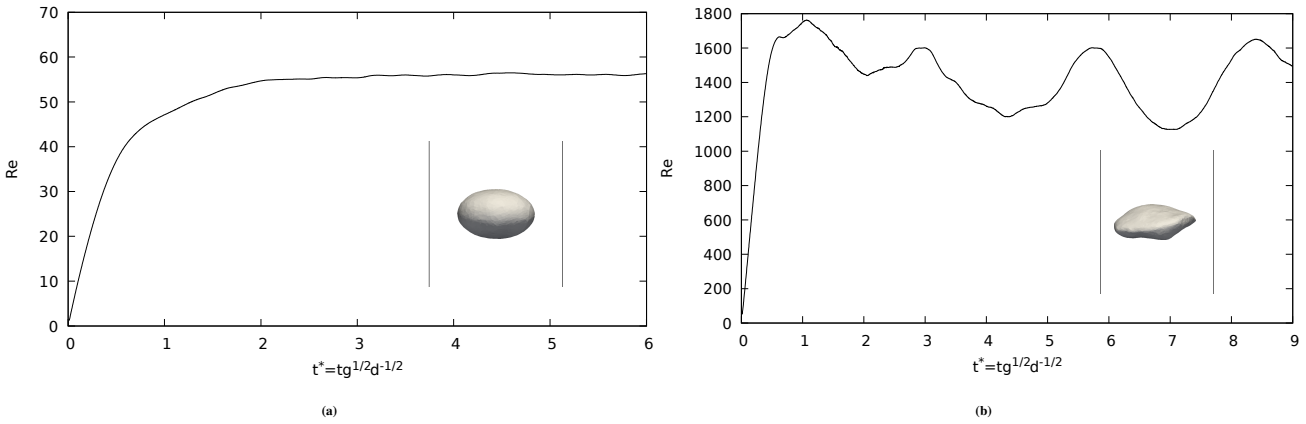

FIGURE 18 Terminal Reynolds number and final shape for (a) $Eo = 3.0$, $logM = -6.0$; (b) $Eo = 11.0$, $M = 2.6e-11$.

As a second validation test in this section, the terminal Re is increased and the dimensionless numbers are depicted in Table 9. The initial mesh, AMR details, initial and boundary conditions are the same as the first test case.

Eo	M	ρ_1/ρ_2	μ_1/μ_2	λ
11.0	$2.6e-11$	100	100	0.50

TABLE 9 Dimensionless numbers for the second validation test.

Figure 18b shows the time evolution for the Reynolds number and the final shape of the bubble, which presents deformations accordingly to the wobbling regime. Experimental and numerical results are compared with our present calculations, regarding the scale factor relation, suggested by[69],

$$SF = U_T/U_M \tag{25}$$

Case $Eo = 11.0$, $M = 2.6e-11$, $\lambda = 0.5$	SF
Experiment[69]	$\sim$ [0.66-0.69]
Eq. (27)[62]	0.65
Numerical simulation[71]	0.69
Present AMR-CLS	0.65

TABLE 10 Present SF computations compared with experimental results by[69], correlation[62] and numerical results by[71].

where U_M is defined by the Mendelson equation[70],

$$U_M = \sqrt{\frac{2\sigma}{\rho_1 d} + \frac{gd}{2}}. \tag{26}$$

Moreover,[62] suggested a correlation for the SF in this regime, given by

$$SF = [1 - (d/D_{cyl})^2]^{3/2}. \tag{27}$$

Our numerical result is presented in Table 10. In the wobbling regime, the velocity tends to oscillate so the terminal average velocity was calculated for SF, by discarding the initial overshoot (startup influences of the simulation) at $t^* = 0.6$. The comparison was made against experiments, correlations and numerics found in the literature, where our result compares fair well with these references.

4.5 | Three-dimensional buoyant bubble in a complex pipe

Pipes with complex configurations, as coiled tubes, are widely present on the nuclear and chemical process due to its compactness in volume and high efficiency in heat transfer[1]. In the earlier section, the methodology was validated with the rising of a bubble in a vertical pipe, where the bubble velocity decreases due to the wall and the bubble deformed into an ellipsoidal shape. In this section, we investigate the rising of a bubble in a complex pipe and the effect of the wall on the rising motion. The dimensionless numbers selected are the same to the case in section 4.2, and are depicted in Table 11.

Eo	M	ρ_1/ρ_2	μ_1/μ_2
4.88	$1.25e-05$	100	100

TABLE 11 Dimensionless numbers for the presented test.

The dimensions of the domain are shown in the figure 19, where the initial bubble of diameter $d = 0.25$ is located at $(x, y, z) = (0, d, 0)$. Moreover, the boundary conditions in the lateral walls are no-slip, whereas the Neumann condition is applied to the top/bottom walls. The initial mesh is around 80k control volumes, and AMR was used to achieve the desired grid resolution ($h = d/60$) in the interface and the near wake at different time moments (See Fig. 19). The final number of control volumes was around 2.2M.

Figure 20 shows the terminal Reynolds number as the bubble travel through the pipe. The bubble rises because of buoyancy, where a pair of counter-rotating vortices appear at the bottom, making a cunning of the lower surface. With this deformation, the surface tension force and the viscous drag are increased, making the bubble to decelerate until reach an equilibrium. However, as the pipe presents a deviation, the bubble reaches the wall, which increments the drag force and the bubble drastically decrease its velocity and changes its shape to more spherical due to the increase of surface tension force provoked by the formation of different vortex near the wall (see Figs. 21 and 20). Along the inclined wall, the velocity and shape keep stable, where a vortex in the contact point between the bubble and the wall prevents its attachment. Moreover, it presents a sliding motion for this inclination angle. Later on, when the bubble gets into a rectilinear section of the pipe, it is velocity increase until it reaches an equilibrium, similar to the first section of the pipe.

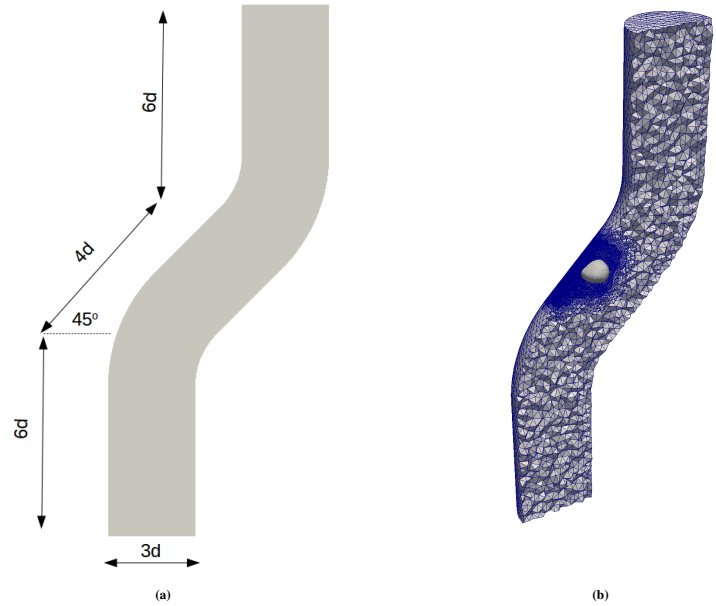

FIGURE 19 (a) Configuration and dimensions of the computational domain. (b) 3D AMR grid for the test case $Eo = 4.88$, $M = 1.25e-05$, with an minimum grid resolution of 60 control volumes per diameter at the interface.

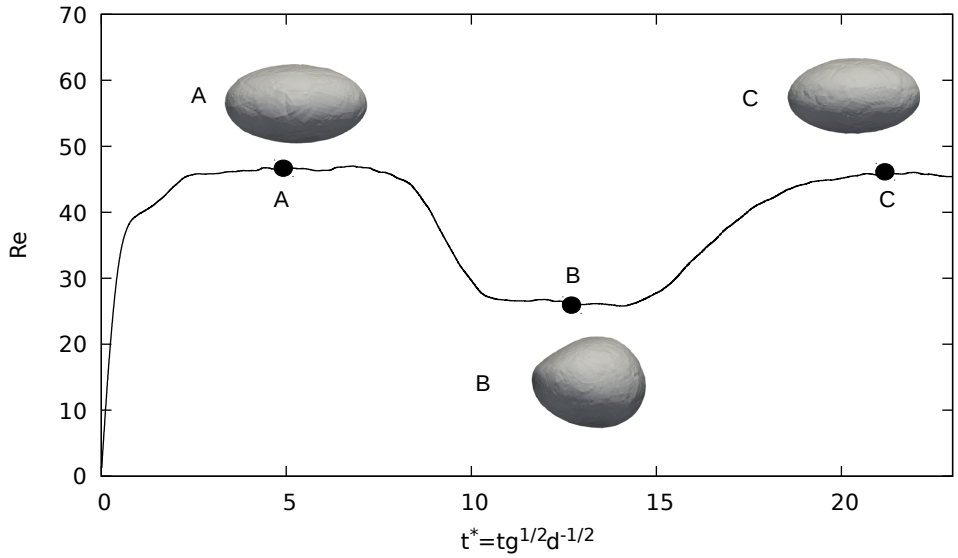

FIGURE 20 Terminal Reynolds number for $Eo = 4.88$, $M = 1.25e-05$.

5 | CONCLUSIONS

In this paper, we introduce a parallel adaptive tetrahedral-mesh refinement algorithm for two-phase flows in complex computational domains. The proposed methodology consisted in the coupling of the tetrahedral Adaptive Mesh Refinement algorithm presented in this work, with a finite-volume / level-set method for collocated unstructured meshes introduced in [16,13,17]. This methodology allows reproducing the main features of three-dimensional two-phase flows with surface tension, combining an accurate representation of the interface, proper mass conservation, and a reduction of the computational effort in comparison

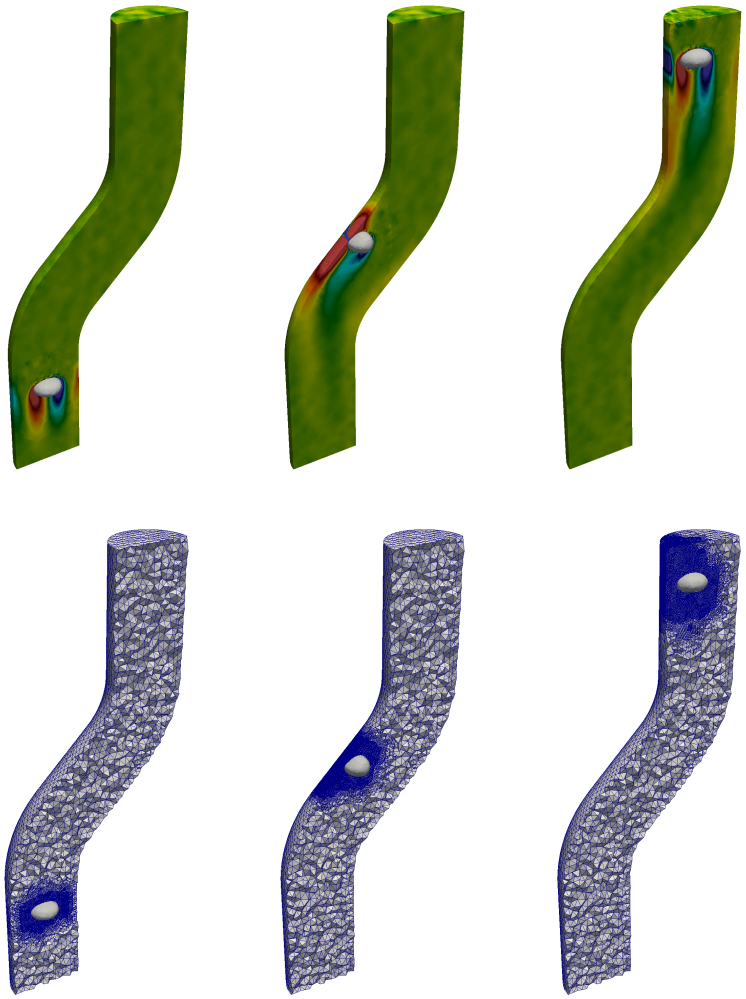

FIGURE 21 Vorticity field and its respective 3D AMR grid for $Eo = 4.88$, $M = 1.25e-05$ at different bubble positions.

with fixed meshes. Moreover, the AMR follows a regular refinement division of the tetrahedron element, taking into account a geometrical criterion to preserve the mesh quality and enabling the use of non-conforming meshes.

Numerical tests involving gravity-driven bubble/droplet in regular and complex domains are used to evaluate the efficacy of the method reported. For the case of the gravity-driven bubble in an infinite domain, the terminal Reynolds number and the aspect ratio compare well with the results of experimental reference. Besides, the use of different convective schemes shows similar results for this case and the mass conservation is preserved. Moreover, the mesh compression, mesh quality and CPU-times were assessed proven the method to be efficient and to keep a proper quality metric.

The methodology was validated against the rising motion of droplets in a pipe, with different diameter ratios, going from deformed spheroidal to Taylor droplets. The numerical results showed the ability to reproduce, in a fair manner, the terminal velocity, and droplet shape when the diameter ratio was increased and the wall effect became significant. In simulations of the gravity-driven bubble in a pipe, the terminal Reynolds number agrees well with the numerical reference using a fixed grid. Moreover, the scale factor, for cases with wall influence, shows good agreement with the experiments, correlation equations and numerical references. Finally, for the test of gravity-driven in a complex domain, terminal Reynolds number, final shape, and flow field are shown. The wall effect produces a decrease in the velocity, increasing the drag forces which makes the bubble to be more spherical. Moreover, the simulation presents an inclined section, where the bubble has shown a sliding motion accordingly to the inclination angle described.

The tests presented indicate that the numerical methods described are quite useful for the direct numerical simulation of two-phase flows in complex domains.

ACKNOWLEDGMENTS

This work has been financially supported by the *Ministerio de Economía y Competitividad, Secretaría de Estado de Investigación, Desarrollo e Innovación*, Spain (ENE2017-88697-R), and by Termo Fluids S.L. Oscar Antepara acknowledges financial support in form of a doctoral scholarship DI-14-06886 of the *Ministerio de Economía y Competitividad* and 2015DI-68 of the *Secretaria d' Universitats i Recerca del Departament d'Economia i Coneixement de la Generalitat de Catalunya*, Spain. Néstor Balcázar acknowledges financial support of the *Programa Torres Quevedo, Ministerio de Economía y Competitividad, Secretaría de Estado de Investigación, Desarrollo e Innovación* (PTQ-14-07186), Spain. Three-dimensional simulations were carried out using computer time provided by PRACE 14th Call (Project 2016153612) and RES project(FI-2018-1-0025) through the MareNostrum IV supercomputer based in Barcelona, Spain. We acknowledge Santander Supercomputacion support group at the University of Cantabria who provided access to the supercomputer Altamira Supercomputer at the Institute of Physics of Cantabria (IFCA-CSIC), member of the Spanish Supercomputing Network, for performing simulations/analyses (RES project FI-2018-3-0037).

Conflict of interest

The authors declare no potential conflict of interests.

References

1. Kong L, Gao X, Li R, Han J. Bubbles in curved tube flows - An experimental study. *International Journal of Heat and Mass Transfer* 2017; 105: 180 - 188.

2. Unverdi S, Tryggvason G. A front-tracking method for viscous, incompressible, multifluid flows. *Journal of Computational Physics* 1992; 100: 25-37.

3. Tryggvason G, Bunner B, Esmaeeli A, et al. A front-tracking method for the computations of multiphase flow. *Journal of Computational Physics* 2001; 169: 708-759.

4. Hirt C, Nichols B. Volume of fluid (VOF) method for the dynamics of free boundary. *Journal of Computational Physics* 1981; 39: 201-225.

5. Scardovelli R, Zaleski S. DIRECT NUMERICAL SIMULATION OF FREE-SURFACE AND INTERFACIAL FLOW. *Annual Review of Fluid Mechanics* 1999; 31(1): 567-603.

6. Van Sint Annaland M, Deen N, Kuipers J. Numerical simulation of gas bubbles behaviour using a three-dimensional volume-of-fluid method. *Chemical Engineering Science* 2005; 60: 2999-3011.

7. Osher S, Sethian J. Fronts propagating with curvature-dependent speed: Algorithms based on Hamilton-Jacobi formulations. *Journal of Computational Physics* 1988; 79: 175-210.

8. Sussman M, Smereka P, Osher S. A Level Set Approach for Computing Solutions to Incompressible Two-Phase Flow. *Journal of Computational Physics* 1994; 144: 146-159.

9. Sussman M, Fatemi E, Smereka P, Osher S. An improved level set method for incompressible two-phase flows. *Computers & Fluids* 1998; 27(5): 663 - 680.

10. Sussman M, Puckett EG. A Coupled Level Set and Volume-of-Fluid Method for Computing 3D and Axisymmetric Incompressible Two-Phase Flows. *Journal of Computational Physics* 2000; 162(2): 301 - 337.

11. Wang Z, Yang J, Koo B, Stern F. A coupled level set and volume-of-fluid method for sharp interface simulation of plunging breaking waves. *International Journal of Multiphase Flow* 2009; 35(3): 227 - 246.

12. Sun D, Tao W. A coupled volume-of-fluid and level-set (VOSET) method for computing incompressible two-phase flows. *International Journal of Heat and Mass Transfer* 2010; 53: 645–655.

13. Balcázar N, Rigola J, Castro J, Oliva A. A level-set model for thermocapillary motion of deformable fluid particles. *International Journal of Heat and Fluid Flow* 2016; 62, Part B: 324-343.

14. Olsson E, Kreiss G. A conservative level set method for two phase flow. *Journal of Computational Physics* 2005; 210: 225-246.

15. Olsson E, Kreiss G, Zahedi S. A conservative level set method for two phase flow II. *Journal of Computational Physics* 2007; 225(1): 785 - 807.

16. Balcázar N, Jofre L, Lehmkhul O, Castro J, Rigola J. A finite-volume/level-set method for simulating two-phase flows on unstructured grids. *International Journal of Multiphase Flow* 2014; 64: 55-72.

17. Balcázar N, Castro J, Rigola J, Oliva A. DNS of the wall effect on the motion of bubble swarms. *Procedia Computer Science* 2017; 108C: 2008-2017.

18. Balcázar N, Lehmkuhl O, Rigola J, Oliva A. A multiple marker level-set method for simulation of deformable fluid particles. *International Journal of Multiphase Flow* 2015; 74: 125-142.

19. Balcázar-Arciniega N, Antepara O, Rigola J, Oliva A. A level-set model for mass transfer in bubbly flows. *International Journal of Heat and Mass Transfer* 2019; 138: 335 - 356.

20. Balcázar-Arciniega N, Rigola J, Oliva A. DNS of Mass Transfer from Bubbles Rising in a Vertical Channel. In: Rodrigues JMF, Cardoso PJS, Monteiro J, et al., eds. *Computational Science – ICCS 2019*Springer International Publishing; 2019; Cham: 596–610.

21. Balcázar N, Lehmkuhl O, Jofre L, Oliva A. Level-set simulations of buoyancy-driven motion of single and multiple bubbles. *International Journal of Heat and Fluid Flow* 2015; 56: 91-107.

22. Berger M. Adaptive mesh refinement for hyperbolic partial differential equations. *Journal of Computational Physics* 1984; 53(3): 484–512.

23. Berger M, LeVeque R. An adaptive cartesian mesh algorithm for the euler equations in arbitrary geometries. *9th Computational Fluid Dynamics Conference, AIAA* 1989.

24. Powell K, Roe PL, Quirk J. Adaptive-mesh algorithms for computational fluid dynamics. *In M. Y. Hussaini, A. Kumar, and M. D. Salas, editors, Algorithmic Trends in Computational Fluid Dynamics* 1993; 53: 303–337.

25. Park M, Krakos J, Michal T, Loseille A, Alonso J. Unstructured grid adaptation: status, potential impacts, and recommended investments toward CFD Vision 2030. 2016.

26. Popiolek T, Awruch A. Numerical simulation of incompressible flows using adaptive unstructured meshes and the pseudo-compressibility hypothesis. *Advances in Engineering Software* 2006; 37(4): 260 - 274.

27. Hoffman J, Jansson J, Abreu dRV, et al. Unicorn: Parallel adaptive finite element simulation of turbulent flow and fluid-structure interaction for deforming domains and complex geometry. *Computers & Fluids* 2013; 80: 310-319.

28. Rossi R, Cotela J, Lafontaine N, Dadvand P, Idelsohn S. Parallel adaptive mesh refinement for incompressible flow problems. *Computers & Fluids* 2013; 80: 342-355.

29. Zheng X, Lowengrub J, Anderson A, Cristini V. Adaptive unstructured volume remeshing - II: Application to two- and three-dimensional level-set simulations of multiphase flow. *Journal of Computational Physics* 2005; 208(2): 626-650.

30. Anderson A, Zheng X, Cristini V. Adaptive unstructured volume remeshing - I: The method. *Journal of Computational Physics* 2005; 208(2): 616-625.

31. Nikolos I, Delis A. An unstructured node-centered finite volume scheme for shallow water flows with wet/dry fronts over complex topography. *Computer Methods in Applied Mechanics and Engineering* 2009; 198(47): 3723 - 3750.

32. Ngo LC, Choi HG. A multi-level adaptive mesh refinement method for level set simulations of multiphase flow on unstructured meshes. *International Journal for Numerical Methods in Engineering*; 110(10): 947-971.

33. Xie Z, Pavlidis D, Percival JR, Gomes JL, Pain CC, Matar OK. Adaptive unstructured mesh modelling of multiphase flows. *International Journal of Multiphase Flow* 2014; 67: 104 - 110.

34. Xie Z, Pavlidis D, Salinas P, Percival JR, Pain CC, Matar OK. A balanced-force control volume finite element method for interfacial flows with surface tension using adaptive anisotropic unstructured meshes. *Computers & Fluids* 2016; 138: 38 - 50.

35. Löhner R. An adaptive finite element scheme for transient problems in CFD. *Computer Methods in Applied Mechanics and Engineering* 1987; 61(3): 323 - 338.

36. Morgan N, Waltz J. 3D level set methods for evolving fronts on tetrahedral meshes with adaptive mesh refinement. *Journal of Computational Physics* 2017; 336: 492-512.

37. Papoutsakis A, Sazhin SS, Begg S, Danaila I, Luddens F. An efficient Adaptive Mesh Refinement (AMR) algorithm for the Discontinuous Galerkin method: Applications for the computation of compressible two-phase flows. *Journal of Computational Physics* 2018; 363: 399 - 427.

38. Giuliani A, Krivodonova L. Adaptive mesh refinement on graphics processing units for applications in gas dynamics. *Journal of Computational Physics* 2019; 381: 67 - 90.

39. Shewchuk J. What Is a Good Linear Finite Element? - Interpolation, Conditioning, Anisotropy, and Quality Measures. *Proceedings of the 11th International Meshing Roundtable* 2002; 73.

40. Freitag L, Ollivier-Gooch C. Tetrahedral mesh improvement using swapping and smoothing. *International Journal for Numerical Methods in Engineering* 1997; 40(21): 3979–4002.

41. Liu A, Joe B. Quality local refinement of tetrahedral meshes based on 8-subtetrahedron subdivision. *Mathematics of Computation* 1996; 65(215): 1183-1200.

42. Peskin C. Numerical analysis of blood flow in the heart. *Journal of Computational Physics* 1977; 25: 220-252.

43. Brackbill J, Kothe D, Zemach C. A continuum method for modeling surface tension. *Journal of Computational Physics* 1992; 100: 335-354.

44. Chang Y, Hou T, Merriman B, Osher S. A level-set formulation of Eulerian interface capturing methods for incompressible two-phase flows. *Journal of Computational Physics* 1996; 124: 462-488.

45. Chorin A. Numerical solution of the Navier-Stokes equations. *Mathematics of Computation* 1968; 22: 745-762.

46. Guermond J, Minev P, Shen J. An overview of projection methods for incompressible flows. *Computer Methods in Applied Mechanics and Engineering* 2006; 195(44): 6011 - 6045.

47. Henk A. VdV, Dekker K. Conjugate gradient type methods and preconditioning. *Journal of Computational and Applied Mathematics* 1988; 24(1): 73 - 87.

48. Karniadakis GE, Kirby II RM. *Parallel Scientific Computing in C and MPI: A Seamless Approach to Parallel Algorithms and their Implementation*. Cambridge University Press . 2003.

49. Rhie C, Chow W. Numerical study of the turbulent flow past an airfoil with trailing edge separation. *AIAA* 1983; 21: 1525-1532.

50. Felten F, Lund T. Kinetic energy conservation issues associated with the collocated mesh scheme for incompressible flow. *Journal of Computational Physics* 2006; 215(2): 465–484.

51. Gottlieb S, Shu C. Total Variation Dimishing Runge-Kutta Schemes. *Mathematics of Computations* 1998; 67: 73-85.

52. Termo Fluids S.L.. http://www.termofluids.com/; .

53. Balcázar N, Lehmkuhl O, Jofre L, Rigola J, Oliva A. A coupled volume-of-fluid/level-set method for simulation of two-phase flows on unstructured meshes. *Computers & Fluids* 2016; 124: 12-29.

54. Antepara O, Balcázar N, Rigola J, Oliva A. Numerical study of rising bubbles with path instability using conservative level-set and adaptive mesh refinement. *Computers & Fluids* 2019; 187: 83 - 97.

55. Gutiérrez E, Balcázar N, Bartrons E, Rigola J. Numerical study of Taylor bubbles rising in a stagnant liquid using a level-set/moving-mesh method. *Chemical Engineering Science* 2017; 164: 158-177.

56. Schillaci E, Jofre L, Balcázar N, Antepara O, Oliva A. A low-dissipation convection scheme for the stable discretization of turbulent interfacial flow. *Computers & Fluids* 2017; 153: 102-117.

57. Schillaci E, Antepara O, Balcázar N, Serrano J, Oliva A. A numerical study of liquid atomization regimes by means of conservative level-set simulations. *Computers & Fluids* 2019; 179: 137-149.

58. Amani A, Balcázar N, Naseri A, Rigola J. A numerical approach for non-Newtonian two-phase flows using a conservative level-set method. *Chemical Engineering Journal* 2020; 385: 123896.

59. Antepara O, Lehmkhul O, Borrell R, Chiva J, Oliva A. Parallel adaptive mesh refinement for large-eddy simulations of turbulent flows. *Computers & Fluids* 2015; 110: 48-61.

60. Favre F, Antepara O, Oliet C, Lehmkuhl O, Perez-Segarra C. An immersed boundary method to conjugate heat transfer problems in complex geometries. Application to an automotive antenna. *Applied Thermal Engineering* 2019; 148: 907 - 928.

61. Karypis G, Schloegel K, Kumar V. ParMETIS, Parallel graph partitioning and sparse matrix ordering library. 1998.

62. Clift R, Grace J, Weber E. Bubbles, Drops and Particles. 1978.

63. Bhaga D, Weber M. Bubbles in viscous liquids: shapes, wakes and velocities. *Journal of Fluid Mechanics* 1981; 105: 61-85.

64. Aoyama S, Hayashi S, Hosokawa A, Tomiyama A. Shapes of ellipsoidal bubbles in infinite stagnant liquids. *International Journal of Multiphase Flow* 2016; 79: 23-30.

65. Sweby P. High resolution using flux limiters for hyperbolic conservation laws. *SIAM Journal on Numerical Analysis* 1984; 21: 995-1011.

66. Gaskell P, Lau A. Curvature-compensated convective transport: SMART a new boundedness-preserving transport algorithm. *International Journal for Numerical Methods in Fluids* 1988; 8: 617-641.

67. Guenther C, Syamlal M. The effect of numerical diffusion on simulation of isolated bubbles in a gas-solid fluidized bed. *Powder Technology* 2001; 116(2): 142 - 154. Modelling and Computational analysis of a collection of particulate and fluid-solid flow problems.

68. Kurimoto R, Hayashi K, Tomiyama A. Terminal velocities of clean and fully-contaminated drops in vertical pipes. *International Journal of Multiphase Flow* 2013; 49: 8 - 23.

69. Krishna R, Urseanu M, Baten vJ, Ellenberger J. Wall effects on the rise of single gas bubbles in liquids. *International Communications in Heat and Mass Transfer* 1999; 26(6): 781 - 790.

70. Mendelson HD. The prediction of bubble terminal velocities from wave theory. *AIChE Journal* 1967; 13(2): 250-253.

71. Mukundakrishnan K, Quan S, Eckmann D, Ayyaswamy P. Numerical study of wall effects on buoyant gas-bubble rise in a liquid-filled finite cylinder. *Phys Rev E Stat Nonlin Soft Matter Phys* 2007; 76(036308).

How to cite this article: O. Antepara, N. Balcázar, and A. Oliva (2020), Tetrahedral adaptive mesh refinement for two-phase flows using conservative level-set method, *XXXX*, *XXXX*.